JACS
JOURNAL OF THE AMERICAN CHEMICAL SOCIETY

pubs.acs.org/JACS
Article

# Mg-Doped Nanosized $BaTaO_2N$ with Long-Lived Charge Carriers toward Efficient Overall Water Splitting

Jing Wang, Jiadong Xiao, Junie Jhon M. Vequizo, Takashi Hisatomi, Mamiko Nakabayashi, Wenpeng Li, Daling Lu, Jingshuai Chen, Naoya Shibata, Akira Yamakata, and Kazunari Domen*

**Cite This:** https://doi.org/10.1021/jacs.6c03784

Read Online

ACCESS | Metrics & More | Article Recommendations | Supporting Information

**ABSTRACT:** Perovskite-type oxynitrides offer a promising route for sustainable solar-to-hydrogen energy conversion via one-step-excitation photocatalytic overall water splitting (OWS). However, insufficient charge carrier lifetimes and sluggish surface reaction kinetics, stemming from inadequate control over bulk and surface properties, have thus far limited photocatalytic efficiency. Herein, we demonstrate that the particle size, defect states, and surface properties of $BaTaO_2N$ can be effectively tailored by combining precursor engineering with Mg doping, thereby enhancing its OWS activity. Mg-doped $BaTaO_2N$ nanocubes with particle sizes of several tens of nanometers were synthesized, and a solar-to-hydrogen energy conversion efficiency an order of magnitude higher than previously reported for $BaTaO_2N$-based photocatalysts was achieved with optimized $IrO_x$ and $Cr_2O_3$/Ru loading. Mechanistic studies reveal that the dual effects of Mg, namely, passivating bulk defects and tuning surface properties, give rise to long-lived charge carriers and efficient transfer of these carriers to uniformly distributed cocatalyst sites. This work demonstrates that precursor engineering combined with Mg doping enables rational bulk−surface coregulation in oxynitride photocatalysts, providing design principles for developing efficient visible-light-driven OWS systems.

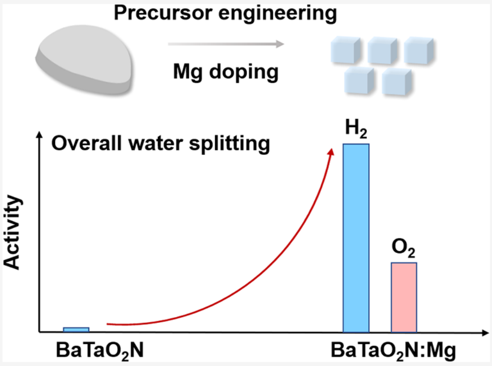

## INTRODUCTION

Harnessing essentially inexhaustible solar energy for one-step overall water splitting (OWS) represents a compelling strategy for sustainable hydrogen production, simultaneously addressing global energy demands and environmental concerns.[1] However, the efficiency of the present-day photocatalysts capable of driving OWS, particularly in response to visible light irradiation, is severely limited.[2,3] Stringent requirements for suitable band gaps and band edge positions also restrict the number of viable visible-light-responsive photocatalysts.[4,5] Even when these criteria are met, rapid charge recombination both in the bulk and at the surface still severely constrains photocatalytic performance.[6] Prolonging charge carrier lifetimes is therefore an essential aspect of achieving efficient OWS, particularly for the oxygen evolution reaction (OER), which involves intrinsically slow multistep kinetics.[7] Existing research strategies typically focus on two main goals: (i) tuning the bulk and surface structures of semiconductors to suppress carrier recombination[2,8] and (ii) employing cocatalysts to accelerate interfacial charge transfer and promote catalytic processes.[3,8,9] Despite these efforts, obtaining long-lived charge carriers while minimizing recombination remains a major challenge. This scenario underscores the importance of developing integrated design strategies that harmonize semiconductor structure, surface properties and cocatalyst function.

Barium tantalum oxynitride ($BaTaO_2N$) is a perovskite-type oxynitride with a narrow band gap (∼1.9 eV) and a potentially high solar-to-hydrogen energy conversion efficiency (STH efficiency) exceeding 10%, such that this compound is a promising visible light OWS photocatalyst.[4,10] Various strategies, including aliovalent $Mg^{2+}$ doping based on $Ta_2O_5$ precursors and precursor engineering with amorphous $Ta_2O_5 \cdot 3H_2O$,[11,12] have enabled visible-light-driven OWS with this material. Nevertheless, the photocatalytic activity of $BaTaO_2N$ remains unsatisfactory, with an STH efficiency of only $5.3 \times 10^{-4}$%.[11,12] This limited performance can be at least partly attributed to the large particles, exceeding 100 nm in size, formed during uncontrolled particle growth that increase the migration paths of photogenerated carriers.[13] The authors' group recently demonstrated that selecting optimal precursors, including the use of $TaS_2$, enables the synthesis of $SrTaO_2N$ nanocrystals with reduced particle sizes and a high degree of crystallinity.[13] Thus, precursor engineering offers a promising

**Received:** February 19, 2026
**Revised:** March 20, 2026
**Accepted:** March 23, 2026

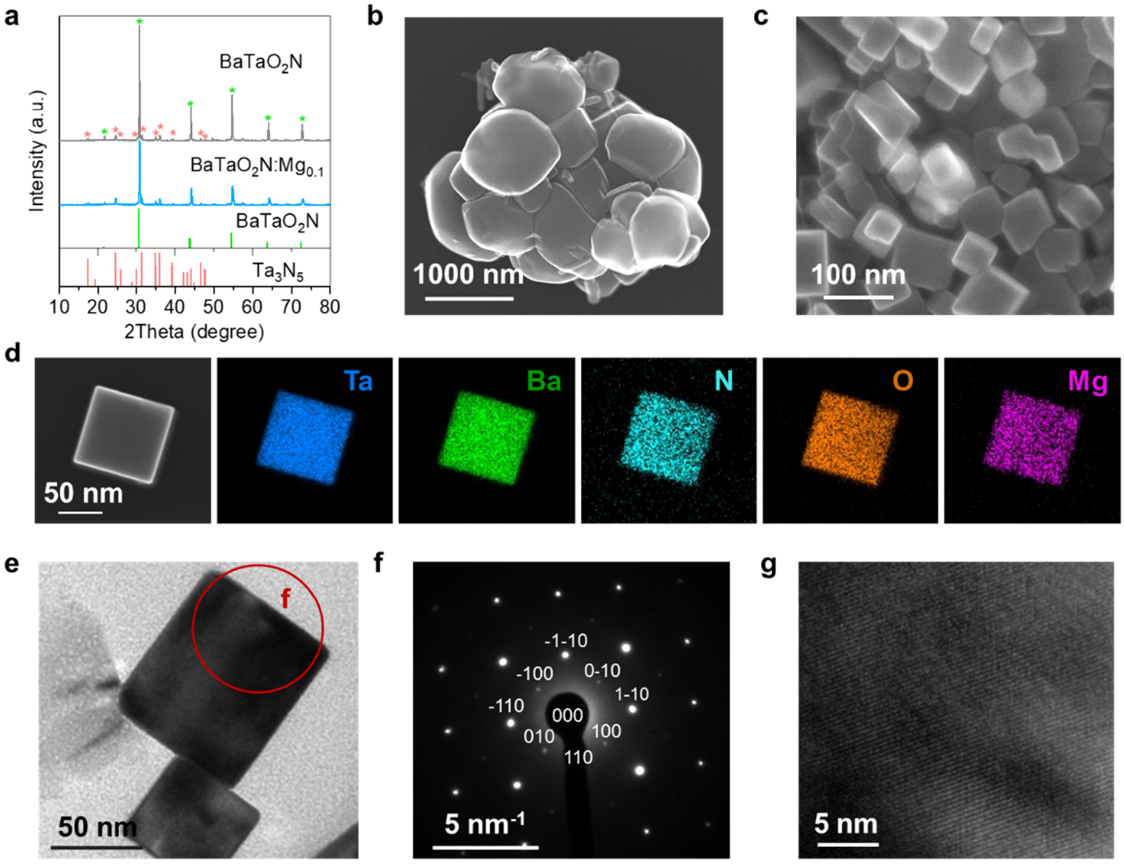

**Figure 1.** Structural and morphological characterization of $BaTaO_2N$ and $BaTaO_2N{:}Mg_{0.1}$. (a) XRD patterns. (b, c) STEM images of (b) $BaTaO_2N$ and (c) $BaTaO_2N{:}Mg_{0.1}$. (d) An ADF-STEM image and corresponding STEM-EDS elemental mapping images of Ta, Ba, N, O and Mg. (e) A cross-sectional TEM image, (f) a SAED pattern, and (g) an HR-TEM image of a $BaTaO_2N{:}Mg_{0.1}$ particle.

approach to controlling photocatalyst particle size, although identifying suitable precursors remains a challenging task.

Formation of the oxynitride phase in $BaTaO_2N$ occurs during high-temperature ammonolysis (nitridation), a process that is often accompanied by the generation of defects comprising reduced Ta species and nitrogen vacancies.[12,14] Despite being widely regarded as recombination centers, the precise structural and functional roles of these defects remain poorly understood.[12] In addition, cocatalysts are also an important aspect of promoting interfacial charge transfer and surface redox reactions, and both the cocatalyst metal and deposition strategy are commonly used to optimize photocatalytic performance. Wang et al. demonstrated that tuning the cocatalyst loading method enables the formation of highly dispersed, uniformly sized Pt sites on $BaTaO_2N$, leading to highly efficient $H_2$ production.[15] However, the effects of the surface properties of $BaTaO_2N$, which can be altered by various modifications and may affect cocatalyst deposition, are often overlooked. Consequently, the pronounced sensitivity of $BaTaO_2N$ performance to the synthesis conditions, combined with a limited understanding of the underlying mechanisms, hinders the rational design of high-performance catalysts for one-step OWS.

To address the intertwined challenges of particle overgrowth, intrinsic defect formation, and inefficient surface charge transfer in $BaTaO_2N$, it will be necessary to simultaneously control particle size along with bulk and surface characteristics while also optimizing the cocatalyst deposition process. Although $TaS_2$ precursor engineering and Mg doping have each been reported as effective approaches for improving oxynitride photocatalysts, these strategies have generally been investigated independently. Adjusting these factors in a coordinated manner is expected to enable efficient OWS reactions. The present work demonstrates that the use of a combination of $TaS_2$, barium hydroxide ($Ba(OH)_2$), a molten salt mixture ($BaCl_2$ and NaCl), and Mg dopants as the nitridation precursors enables the fabrication of Mg-doped $BaTaO_2N{:}Mg$ ($BaTaO_2N{:}Mg$) nanocrystals having an average particle size of approximately 70 nm. Following the loading of $IrO_x$ and $Cr_2O_3/Ru$ cocatalysts, the resulting photocatalyst exhibited an STH efficiency of $5 \times 10^{-3}\%$ that exceeded all values reported to date for $BaTaO_2N$. Each component in the precursor system played a crucial role in producing $BaTaO_2N{:}Mg$ capable of OWS. In particular, doping with Mg had multiple positive effects on the bulk and surface properties of the $BaTaO_2N$, as well as on the interface of this compound with the cocatalysts.

## ■ RESULTS AND DISCUSSION

$BaTaO_2N$ doped with Mg at Ta sites as produced in this work is denoted herein as $BaTaO_2N{:}Mg_x$, where $x$ is the Mg/Ta molar ratio in the initial precursor mixture. $BaTaO_2N{:}Mg_{0.1}$ was synthesized by nitriding a mixture of $TaS_2$, $Ba(OH)_2\cdot 8H_2O$, $BaCl_2$, NaCl and $MgCl_2$ powders combined in a molar ratio of 1:2:0.25:1:0.1 under a flow of $NH_3$ at 1223 K for 3 h (see the Methods section for details). Undoped $BaTaO_2N$ was prepared in the identical manner but without adding the Mg source. Analyses by X-ray photoelectron spectroscopy (XPS) confirmed that neither Na nor Cl was present on the $BaTaO_2N:Mg_{0.1}$ surfaces following synthesis (Figure S1). X-ray diffraction (XRD) patterns obtained from both undoped $BaTaO_2N$ and $BaTaO_2N:Mg_x$ samples (Figures 1a and S2) could be indexed to a perovskite-type $BaTaO_2N$ structure. A minor $Ta_3N_5$ phase was detected in all samples, regardless of the Mg/Ta ratio, and persisted despite extensive optimization of the Ba/Ta precursor ratio, flux type, and nitridation temperature and duration (Figure S3). A slight shift in the positions of the diffraction peaks toward higher angles was observed with increasing Mg content, indicating a lattice contraction of the $BaTaO_2N$. This effect was attributed to the requirement for charge compensation in association with the substitution of $Mg^{2+}$ for $Ta^{5+}$. This occurred via the partial replacement of $N^{3-}$ ions with smaller $O^{2-}$ ions, leading to a reduced lattice parameter.[16,17]

$BaTaO_2N$ primarily formed large, micron-sized particles with an average size of approximately 600 nm (Figure S4a) that were characterized by rounded polyhedral morphologies and smooth, curved surfaces (Figure 1b). This shape indicates pronounced facet rounding during crystal growth. Some particles also exhibited well-defined, near-cubic polyhedral shapes featuring distinct flat facets and terrace-like surface features (Figure S5). Upon doping with Mg, the particle surfaces showed enhanced faceting and smaller, more uniform cubic-like grains were generated with an average size on the order of 70 nm (Figure S4b). These grains were characterized by distinct edges and planar faces (Figure 1c). This outcome contrasts with the results of previous work by the authors, in which the incorporation of Mg had a negligible effect on particle size.[11] This discrepancy can possibly be ascribed to the use of a $TaS_2$-based precursor and to the smaller amount of molten salt employed in this study, in contrast to the oxygen-rich $Ta_2O_5/BaCO_3$ system used previously. The precursor chemistry likely influences the nucleation pathway during nitridation, thereby enabling Mg incorporation to more effectively suppress grain growth and promote the formation of smaller particles. In the present experiments, the relative decrease in the amount of oxygen sources and the flux likely constrained the dissolution and reprecipitation process, leading to the formation of aggregated particles. The pronounced effect of Mg doping suggests that doping altered the crystallization behavior and growth kinetics during nitridation, thereby modulating both particle size and faceting. Notably, the reduced particle size observed after Mg doping may also contribute to the photocatalytic performance, as smaller particles can shorten the charge migration distance.

Elemental mapping performed by annular dark-field scanning transmission electron microscopy (ADF-STEM) in conjunction with energy-dispersive X-ray spectroscopy (EDS) (Figure 1d) confirmed the homogeneous spatial distributions of Ba, Ta, O, N and Mg throughout the particles. It is therefore evident that uniform Mg doping was accomplished with the absence of any surface segregation. The selected-area electron diffraction (SAED) pattern collected from a specific region of a cuboidal $BaTaO_2N:Mg_{0.1}$ particle (Figure 1e) exhibited sharp, well-defined diffraction spots, indicating a high degree of crystallinity (Figure 1f). The absence of diffraction rings or spot splitting establishes that there was minimal structural distortion in the particle, consistent with a cubic crystal structure. Further evidence was provided by cross-sectional high-resolution transmission electron microscopy (HR-TEM) observations of the $BaTaO_2N:Mg_{0.1}$, which revealed well-aligned lattice fringes throughout the entire particle (Figure 1g), indicating high crystallinity across the bulk.

The diffuse-reflectance spectra of $BaTaO_2N$ and $BaTaO_2N:Mg_x$, presented in Figure S6a, confirm that all samples showed an onset of light absorption at 600 nm or longer wavelengths. The slight blue shift of the absorption edge with increasing Mg content indicated tuning of the band-edge states.[16] Variations in the Kubelka−Munk values across the samples were also observed in the near-infrared region (above 700 nm) (Figure S6b), with the undoped $BaTaO_2N$ showing higher values than the Mg-doped counterparts. This near-infrared adsorption is commonly associated with light absorption from defect-related midgap states or impurities.[9,12] Therefore, the introduction of Mg evidently inhibited the formation of defect states, with an optimal effect observed in the case of the $BaTaO_2N:Mg_{0.1}$. A comparison of $BaTaO_2N:Mg_{0.1}$ specimens synthesized using different fluxes (Figure S7) confirmed that the absorption edge was unchanged. However, the flux-free sample exhibited a pronounced band-tail extending from the band edge while the flux-assisted materials showed a sharper absorption onset, indicating reduced defect concentrations. These observations suggest that Mg doping and the flux played complementary roles in suppressing defect formation.

Reduced Ta species ($Ta^{4+}$), the presence of which was evaluated via the deconvolution of Ta 4f XPS spectra (Figure S8), were the primary defects suppressed by Mg doping. The quantitative data regarding surface Ta species derived from the XPS peak areas (Table S1) revealed that the proportion of $Ta^{4+}$ was initially decreased following Mg doping, reaching a minimum in $BaTaO_2N:Mg_{0.1}$, and then slightly increased at higher Mg levels. This trend parallels the intensity of the background absorption in the near-infrared region, which was also minimized in the case of $BaTaO_2N:Mg_{0.1}$. Moreover, the addition of Mg increased the O/Ta ratio in the bulk of the material (Table S1). This effect further inhibited the formation of defect states because the more electronegative $O^{2-}$ ions strengthened the local crystal fields of the $Ta(O,N)_6$ octahedra.[12,16−18] The overall Ta valence state was further evaluated using elemental analysis to estimate the average oxidation state of Ta in the specimens based on the total elemental compositions. In this procedure, the $BaTaO_2N:Mg_x$ samples were assumed to contain perovskite-type oxynitride as the main phase, accompanied by a minor amount of $Ta_3N_5$ as an impurity, and the average Ta valence was calculated based on charge neutrality using the experimentally determined elemental ratios (Table S2). Based on this assumption, the introduction of 10 mol % Mg relative to the amount of Ta would be expected to increase the average Ta valence from +4.97 in $BaTaO_2N$ to +5.00 in $BaTaO_2N:Mg_{0.1}$, which is qualitatively consistent with the XPS results. In addition to the suppressed formation of reduced Ta species, Mg doping also modified the surface chemical state of oxygen species. The XPS O 1s spectra acquired from the $BaTaO_2N$ and $BaTaO_2N:Mg_{0.1}$ showed two main components at 529 and 531 eV, corresponding to lattice oxygen ($O^{2-}$) and surface hydroxyl groups ($OH^-$), respectively (Figure S9). Upon Mg doping, the relative proportion of $OH^-$ was increased, suggesting enhanced surface hydrophilicity (Table S1).[16,19] This effect was corroborated by contact-angle measurements showing that $BaTaO_2N:Mg_{0.1}$ provided a smaller contact angle than $BaTaO_2N$ (Figure S10).

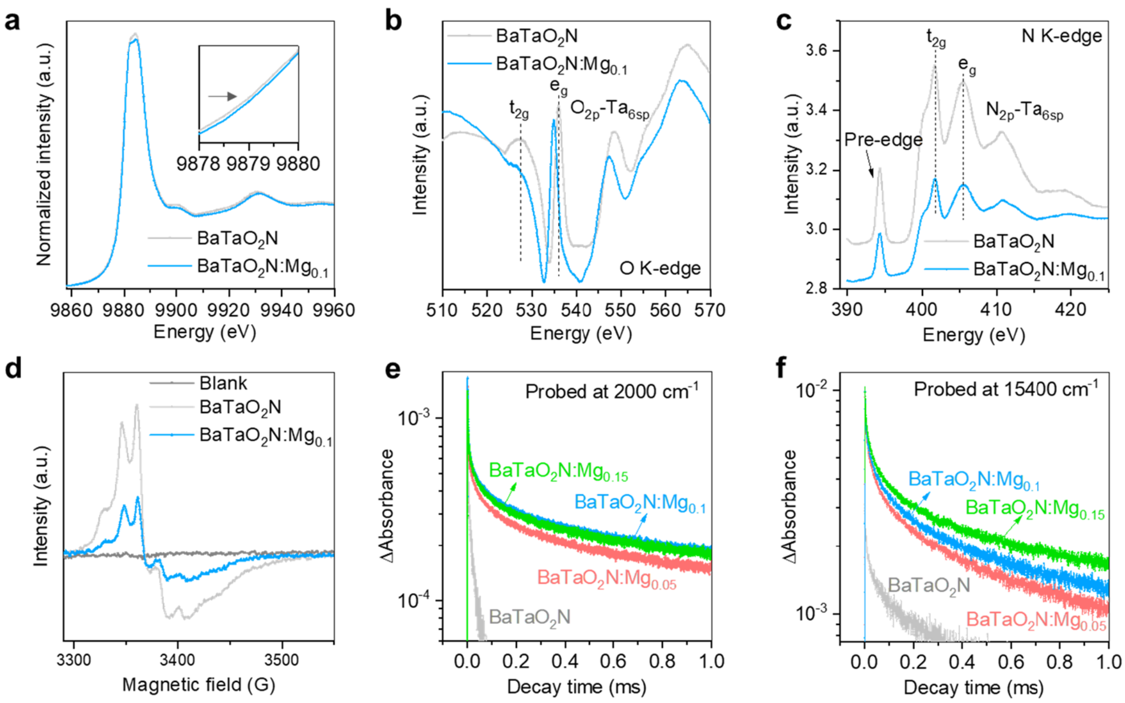

**Figure 2.** (a) Ta L-edge spectra obtained from $BaTaO_2N$ and $BaTaO_2N{:}Mg_{0.1}$. (b) O K-edge and (c) N K-edge XAS spectra obtained from $BaTaO_2N$ and $BaTaO_2N{:}Mg_{0.1}$. (d) EPR spectra of $BaTaO_2N$ and $BaTaO_2N{:}Mg_{0.1}$. Transient decay profiles for photogenerated electrons and holes in $BaTaO_2N$ and $BaTaO_2N{:}Mg_x$ probed at (e) 2000 and (f) 15,400 $cm^{-1}$, respectively.

Changes in the chemical states of the constituent elements of $BaTaO_2N$ induced by Mg doping were assessed by analyzing the undoped material and $BaTaO_2N{:}Mg_{0.1}$ using X-ray absorption spectroscopy (XAS). The resulting Ta K-edge XAS data showed that the absorption edge of $BaTaO_2N{:}Mg_{0.1}$ was positively shifted compared with that of $BaTaO_2N$, confirming that changes in the valence state of TA in the bulk material resulted from Mg incorporation (Figure 2a). The combined XPS and XAS results established that the addition of Mg stabilized the $Ta^{5+}$ state by inhibiting reduction. The O K-edge XAS spectrum acquired from $BaTaO_2N$ contained two distinct pre-edge features at approximately 529 and 533 eV (Figure 2b), corresponding to excitations from the O 1s core level to hybridized O 2p−Ta 5d $t_{2g}$ and $e_g$ states, respectively, reflecting the octahedral coordination of $Ta^{5+}$ ($5d^0$).[20] Mg doping shifted these features to lower energies, suggesting a reduced oxidation state in the oxide ions. This finding was in agreement with the evident increase in the average Ta valence state and the stronger local crystal field experienced by O atoms in the photocatalyst. The intensities of these peaks were also increased, indicating enhanced ligand-field definition and improved local structural order.[21] The higher-energy region associated with O 2p−Ta 6sp antibonding states also showed increased spectral weight. Hence, it appears that the degree of covalency in Ta−O bonds was increased, in keeping with the increased O/Ta ratios following Mg incorporation.[21] The N K-edge XANES spectra exhibited well-resolved near-edge peaks attributed to transitions from the N 1s core level to the Ta 5d $t_{2g}$ and $e_g$ states, with broader resonances at higher energies corresponding to N 2p−Ta 6sp hybridized states (Figure 2c).[20] Notably, the pre-edge intensity, which has been previously linked to defect-induced localized states such as nitrogen vacancies,[22,23] was decreased following Mg doping. This result paralleled the lower proportion of reduced Ta species (that is, $Ta^{4+}$) suggested by the XPS data and the suppression of background absorption in the near-infrared region.[23] From this trend, it is evident that Mg incorporation affected the Ta valence state and also stabilized local $Ta(O,N)_6$ octahedra, thereby limiting the formation of nitrogen-based defect states.

Electron paramagnetic resonance (EPR) spectroscopy performed at 77 K was employed to assess defects in the materials (Figure 2d). The analysis of blanks generated negligible signals, confirming that the observed features originated from the oxynitrides. All samples produced weak EPR signals at $g = 2.056 \pm 0.001$ accompanied by partially resolved hyperfine splitting. It is unlikely that these features were related to $Ta^{4+}$ species, which typically provide $g$ values significantly different from 2 and strong anisotropic line broadening due to a high degree of spin−orbit coupling.[24] Instead, the observed resonance can be more reasonably attributed to defect states associated with nitrogen vacancies. Unpaired electrons are primarily localized at these vacancy sites but also partially delocalized to neighboring Ta(V) centers. These characteristics are consistent with those previously reported for ligand-centered radical states in $d^0$ tantalum complexes. In such states, unpaired electrons are largely decoupled from the metal centers but still produce weak hyperfine Ta interactions.[25] Compared with $BaTaO_2N$, $BaTaO_2N{:}Mg_{0.1}$ showed a substantial reduction in nitrogen vacancies, confirming that Mg doping played a clear role in locally passivating defects, in agreement with the XPS and XAS analyses.

Time-resolved absorption spectra (TAS) were acquired at 2000 and 15,400 $cm^{-1}$ following band gap excitation ($\lambda_{pump}$ = 480 nm, 2.58 eV) to probe changes in the charge carrier dynamics upon Mg doping (Figure 2e and 2f). These frequencies correspond to the signals for free or shallowly trapped electrons and photoinduced trapped holes, respectively.[26] Undoped $BaTaO_2N$ exhibited the weakest TAS

https://doi.org/10.1021/jacs.6c03784
J. Am. Chem. Soc. XXXX, XXX, XXX−XXX

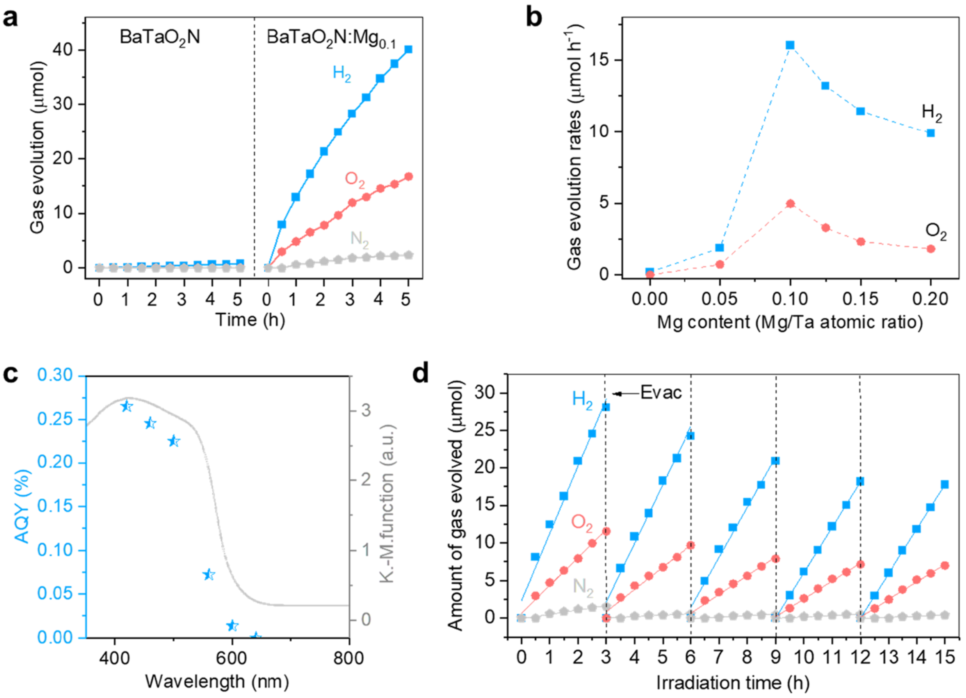

**Figure 3.** (a) Photocatalytic activity of $BaTaO_2N$:Mg. Evolution of $H_2$, $O_2$ and $N_2$ over time using $BaTaO_2N$ or $BaTaO_2N:Mg_{0.1}$ under visible light ($\lambda \geq 420$ nm). (b) Data showing the OWS activity of $BaTaO_2N:Mg_x$ specimens with various Mg/Ta ratios. (c) Action spectrum of $BaTaO_2N:Mg_{0.1}$ for the OWS reaction along with the UV−vis diffuse reflectance spectrum for comparison. (d) Data from extended cycles of OWS reactions over $BaTaO_2N:Mg_{0.1}$ under visible light ($\lambda \geq 420$ nm).

intensity at 2000 $cm^{-1}$ together with a rapid signal decay, attributable to rapid electron trapping in deep states. These states likely correspond to reduced Ta species and nitrogen vacancies acting as recombination centers. Subsequent to Mg incorporation, the TAS signals became markedly stronger and the decay kinetics slowed, indicating suppressed carrier recombination due to the effective passivation of deep-level defects. $BaTaO_2N:Mg_{0.1}$, which contained the fewest reduced Ta species, showed the highest electron TAS intensity and the slowest decay. The signal related to holes at 15,400 $cm^{-1}$ showed a similar trend of suppressed recombination, with $BaTaO_2N:Mg_{0.15}$ (which had the highest Mg content) exhibiting the longest hole lifetime. These results demonstrate that Mg doping effectively reduced the number of recombination centers, thus enhancing both electron and hole retention. However, the optimal levels of Mg doping required to maximize the electron and hole lifetimes differed slightly. It should be noted that the carrier lifetimes obtained from TAS measurements under an $N_2$ atmosphere primarily reflect charge recombination dynamics rather than the kinetics of surface catalytic reactions, and therefore do not necessarily indicate the rate-determining step in the overall water splitting reaction.

After sequential modification with optimized $IrO_x$ and $Cr_2O_3$/Ru (nominally Ir 0.3 wt %, Ru 4 wt %, and Cr 4%) (Figure S11),[9] $BaTaO_2N:Mg_{0.1}$ evolved both $H_2$ and $O_2$ in photocatalytic OWS trials under visible light illumination ($\lambda >$ 420 nm). These trials provided initial $H_2$ and $O_2$ evolution rates of 16 and 5.7 $\mu$mol $h^{-1}$, respectively (Figure 3a). While the $H_2$:$O_2$ molar ratio initially deviated from the expected stoichiometric value of 2:1, this ratio gradually approached the expected stoichiometric value over time. In contrast, $BaTaO_2N$ was found to be inactive when applied to the OWS reaction. Systematic variation of the Mg concentration in these specimens demonstrated that both lower and higher Mg levels relative to that in $BaTaO_2N:Mg_{0.1}$ reduced the OWS activity, especially in the case of lower Mg contents (Figure 3b). Furthermore, $BaTaO_2N:Mg_{0.1}$ exhibited water splitting activity when synthesized using KCl, RbCl or CsCl as the flux rather than NaCl (Figure S12a), whereas the undoped samples remained inactive regardless of the flux used (Figure S12b). The lack of activity in the absence of Mg doping indicates that the incorporation of this metal was the primary factor enabling OWS activity, while the flux played a secondary role in tuning the overall performance.

Using the optimized conditions, $BaTaO_2N:Mg_{0.1}$ provided an apparent quantum yield (AQY) of 0.27% at 420 nm. The onset of the AQY action spectrum was also consistent with that of the diffuse reflectance spectrum (Figure 3c). The STH efficiency in the initial stage of the reaction was determined to be $5.3 \times 10^{-3}$%, which is approximately an order of magnitude higher than values previously reported for $BaTaO_2N$ and Mg-doped $BaTaO_2N$ OWS photocatalysts.[11,12] The stability of $BaTaO_2N:Mg_{0.1}$ was assessed by applying visible light to the material for an extended duration with periodic degassing. As shown in Figure 3d, although the activity gradually decreased over successive cycles, likely due to minor leaching of the surface cocatalyst, the photocatalyst continued to produce both hydrogen and oxygen under the test conditions. The constant binding energies observed in XPS spectra obtained from the specimen confirmed that the chemical states of the Ta lattice and the Ir and Ru cocatalysts remained unchanged throughout the prolonged reaction (Figure S13a−c). Further evidence for the robust nature of the catalyst was provided by XRD analyses (Figure S13d) that showed no detectable changes in the $BaTaO_2N:Mg_{0.1}$ crystal structure. Together, these data confirm the absence of both surface chemical reactions and bulk structural degradation during the OWS process.

https://doi.org/10.1021/jacs.6c03784
J. Am. Chem. Soc. XXXX, XXX, XXX−XXX

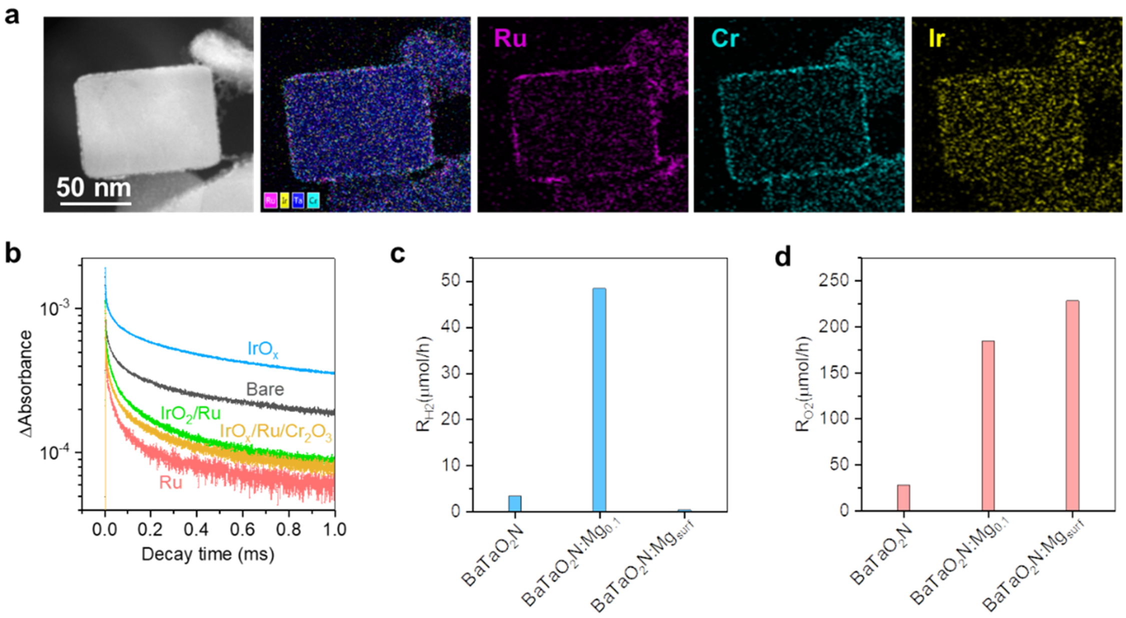

**Figure 4.** (a) ADF-STEM images and STEM-EDS elemental maps of a cross-sectional sample of a $BaTaO_2N:Mg_{0.1}$ specimen loaded with $IrO_x$ and $Ru/Cr_2O_3$ cocatalysts. (b) Transient decay profiles for photogenerated electrons in $BaTaO_2N:Mg_{0.1}$ probed at 2000 $cm^{-1}$. (c) $H_2$ and (d) $O_2$ evolution rates for $BaTaO_2N$, $BaTaO_2N:Mg_{0.1}$ and $BaTaO_2N:Mg_{surf}$ samples loaded with $Ru/Cr_2O_3$ and Ir cocatalysts.

**Table 1. Half-Reaction Activities of $BaTaO_2N:Mg_{0.1}$ Specimens with Various Cocatalyst Modifications**

| | cocatalyst[a] | | | | activity | |
|---|---|---|---|---|---|---|
| entry | Ir (MW) | Ru (IMP) | $H_2$-treated | Cr (PD) | HER[b]/μmol $h^{-1}$ | OER[c]/μmol $h^{-1}$ |
| 1 | √ | √ | √ | √ | 37 | 79 |
| 2 | – | √ | √ | √ | 48 | 10 |
| 3 | – | √ | √ | – | 24 | 22 |
| 4 | √ | √ | √ | | 28 | 160 |
| 5 | √ | – | √ | √ | 0 | 151 |
| 6 | √ | – | √ | – | 0 | 185 |
| 7 | √ | – | – | – | 0 | 14 |
| 8 | – | – | – | – | 0 | 0 |

[a] MW, IMP, and PD denote cocatalysts loaded by microwave-assisted synthesis, impregnation, and photodeposition, respectively; $H_2$-treated indicates postreduction under an $H_2$ atmosphere at 250 °C. Ir, Ru, and Cr represent the corresponding metal cocatalysts loaded on the photocatalyst, with loadings of 0.3 wt % Ir, 4.0 wt % Ru, and 4.0 wt % Cr. A check mark (√) indicates the presence of the corresponding cocatalyst or treatment. [b] $CH_3OH$ aq ($\lambda > 420$ nm) [c] $AgNO_3$ aq ($\lambda > 420$ nm).

Cocatalysts play a crucial role in facilitating surface redox reactions during photocatalytic OWS. Cross-sectional ADF-STEM observations established that the $IrO_x$ and $Cr_2O_3/Ru$ cocatalysts were densely and uniformly deposited on the $BaTaO_2N:Mg_{0.1}$ surfaces (Figure 4a), achieving a high degree of surface coverage. EDS images also showed that Ir and Ru uniformly covered the entire surfaces of the photocatalyst particles. It is thought that Cr species were deposited as an overlayer that encapsulated the Ru regions,[9] although the limited magnification of the present instrumentation prevented the direct observation of this effect.

The individual and synergistic contributions of the cocatalysts were evaluated by assessing the half-reaction activities of $BaTaO_2N:Mg_{0.1}$ particles loaded with different cocatalysts. Table 1 summarizes the effects of these cocatalyst modifications based on sequentially applying Ir (MW, microwave), Ru (IMP, impregnation), $H_2$ reduction treatment and $Cr_2O_3$ (PD, photodeposition). The Ru-loaded samples exhibited appreciable $H_2$ evolution activity, which was further enhanced by Cr coloading. This effect can presumably be attributed to improved charge transfer at the interface resulting from the $Cr_2O_3$ layer.[27] In contrast, Ir loading alone showed negligible $H_2$ evolution activity, confirming that Ru served as the primary cocatalyst for proton reduction. Notably, coloading both Ir and Ru significantly increased the $H_2$ evolution rate. The Ir-loaded samples subjected to $H_2$ reduction exhibited significantly higher $O_2$ evolution rates compared with the materials without Ir or with unreduced Ir. Moreover, Ru and Cr, whether loaded individually or in combination, resulted in lower $O_2$ evolution rates. These results strongly suggest that Ru and $IrO_x$ served as the dominant active components for $H_2$ and $O_2$ evolution, respectively, in the $BaTaO_2N:Mg_{0.1}$ system, in agreement with earlier studies of comparable cocatalyst systems.[9,13]

To further elucidate the roles of the various cocatalysts, the effects of $IrO_x$ (after $H_2$ reduction), $Ru/IrO_x$ and $Cr_2O_3/Ru/IrO_x$ as cocatalysts were examined using TAS with probing at 2000 $cm^{-1}$ (5000 nm, approximately 0.24 eV).[9] As shown in Figure 4b, loading $IrO_x$ onto $BaTaO_2N:Mg_{0.1}$ increased the electron population and prolonged the electron lifetimes compared with the bare sample. This effect was likely due to rapid hole capture that suppressed charge carrier recombination. Given that electrons are readily consumed during $Ag^+$ reduction, this is consistent with the enhanced sacrificial OER activities. Subsequent Ru loading accelerated electron decay beyond that of the bare $BaTaO_2N:Mg_{0.1}$, indicating rapid electron transfer to Ru. The additional loading of Cr on the $IrO_x$/Ru system accelerated electron decay further, in line with the superior $H_2$ evolution activity following this modification.

Notably, Mg incorporation not only suppressed bulk defects but also modified the surface electronic structure and interfacial properties of the $BaTaO_2N$, both of which affect photocatalytic performance. ADF-STEM observations confirmed that the Ru nanoparticles were more densely and uniformly distributed on the $BaTaO_2N:Mg_{0.1}$ surfaces, whereas the Ru species on $BaTaO_2N$ were unevenly dispersed with signs of partial aggregation (Figure S14a,b). A similar trend was observed in the case of the $IrO_x$-loaded samples (Figure S14c,d). These results suggest that Mg-induced surface modifications facilitated cocatalyst nucleation and anchoring, likely through improved wettability and altered surface chemistry.[28]

The ability of Mg doping to simultaneously modulate both the bulk and surface properties of $BaTaO_2N$ in a favorable manner is of paramount importance in photocatalyst design. Even though surface properties can be controlled through the postloading of dopants via the surface, the bulk properties of $BaTaO_2N$ are not fundamentally improved in this manner, thereby failing to achieve truly enhanced photocatalytic activity. This effect was assessed by comparing $BaTaO_2N:Mg_{0.1}$ with its surface-modified counterpart ($BaTaO_2N:Mg_{surface}$) prepared by loading $MgCl_2$ (10 mol %) onto undoped $BaTaO_2N$. Surface modification alone did not effectively suppress defect-related electronic states, although it did improve surface hydrophilicity (Figure S10). This result provides additional evidence that the incorporation of Mg into the bulk of the catalyst is essential for defect passivation and electronic structure optimization (see Figure S15 for details).

As shown in Figure 4c,d, $BaTaO_2N:Mg_{0.1}$ exhibited significantly enhanced $H_2$ and $O_2$ evolution activities compared with pristine $BaTaO_2N$, highlighting the critical role of bulk Mg incorporation in improving charge carrier utilization. $BaTaO_2N:Mg_{surf}$ also showed a pronounced increase in $O_2$ evolution activity, reaching 200 $\mu$mol $h^{-1}$. This value was more than an order of magnitude higher than that obtained for pristine $BaTaO_2N$ and even exceeded that shown by $BaTaO_2N:Mg_{0.1}$. Hence, it is evident that surface modification with Mg facilitated hole utilization for water oxidation, likely by increasing the surface hydrophilicity of the $BaTaO_2N$ and optimizing the interfacial reaction environment. However, the TAS data established that surface Mg modification had a negligible effect on bulk electron dynamics (Figure S15f). Furthermore, this modification did not improve the HER activity and even led to a slight decrease, consistent with the minimal changes observed in reduced Ta species and electron lifetimes. Consequently, $BaTaO_2N:Mg_{surf}$ did not exhibit OWS activity under the same cocatalyst configuration (Figure S16), despite the enhanced $O_2$ evolution performance of this material after $IrO_x$ loading. This finding provides further evidence that surface Mg modification alone is insufficient to establish the electronic requirements for simultaneous $H_2$ and $O_2$ evolution, as the unbalanced half-reaction kinetics cannot sustain steady-state OWS. Instead, bulk Mg incorporation is indispensable for defect passivation and for prolonged charge-carrier lifetimes, which together enable balanced redox processes.

## ■ CONCLUSIONS

A rational synthesis strategy that combines precursor selection with controlled Mg doping enabled the fabrication of cubic $BaTaO_2N:Mg_{0.1}$ photocatalysts showing markedly enhanced performance. Mg doping induced a morphological transformation from large irregular particles to well-defined nanocubes, while simultaneously suppressing detrimental defects and extending carrier lifetimes. These changes effectively promoted charge separation and migration. In addition, the incorporation of Mg enhanced the surface hydrophilicity, consistent with the effect of surface Mg loading. Such surface modification is also favorable for the dispersion of $IrO_x$ and $Cr_2O_3$/Ru cocatalysts, thereby further facilitating charge separation, migration, and interfacial transfer. With optimized cocatalyst loading, $BaTaO_2N:Mg_{0.1}$ provided an STH efficiency of $5.3 \times 10^{-3}$% in the early stage of the OWS reaction, nearly an order of magnitude higher than that obtained from undoped $BaTaO_2N$. These results highlight the central role of Mg-induced morphology control, defect regulation and interface engineering in oxynitride photocatalysts, providing general design principles for advancing solar-driven OWS.

## ■ ASSOCIATED CONTENT

### Supporting Information

The Supporting Information is available free of charge at https://pubs.acs.org/doi/10.1021/jacs.6c03784.

Experimental section; additional characterization and reaction results (PDF)

## ■ AUTHOR INFORMATION

### Corresponding Author

**Kazunari Domen** − *Institute for Aqua Regeneration, Shinshu University, Nagano 380-8553, Japan; Office of University Professors, The University of Tokyo, Tokyo 113-8565, Japan*; orcid.org/0000-0001-7995-4832; Email: domen@chemsys.t.u-tokyo.ac.jp

### Authors

**Jing Wang** − *Institute for Aqua Regeneration, Shinshu University, Nagano 380-8553, Japan*; orcid.org/0000-0001-8024-1880

**Jiadong Xiao** − *Research Initiative for Supra-Materials, Interdisciplinary Cluster for Cutting Edge Research, Shinshu University, Nagano 380-8553, Japan; School of Chemical Engineering, University of Chinese Academy of Sciences, Beijing 101408, China*; orcid.org/0000-0001-9130-5376

**Junie Jhon M. Vequizo** − *Institute for Aqua Regeneration, Shinshu University, Nagano 380-8553, Japan*; orcid.org/0000-0003-2490-2335

**Takashi Hisatomi** − *Institute for Aqua Regeneration, Shinshu University, Nagano 380-8553, Japan*; orcid.org/0000-0002-5009-2383

**Mamiko Nakabayashi** − *Institute of Engineering Innovation, School of Engineering, The University of Tokyo, Tokyo 113-8656, Japan*

**Wenpeng Li** − *Institute for Aqua Regeneration, Shinshu University, Nagano 380-8553, Japan; Shanxi Key*

*Laboratory of Catalysis and Energy Coupling, College of Chemical Engineering and Technology, Taiyuan University of Science and Technology, Taiyuan 030024, China*

**Daling Lu** − *Institute for Aqua Regeneration, Shinshu University, Nagano 380-8553, Japan*

**Jingshuai Chen** − *School of Chemistry and Chemical Engineering, Anhui University, Hefei 230601, China;* orcid.org/0009-0007-6741-563X

**Naoya Shibata** − *Institute of Engineering Innovation, School of Engineering, The University of Tokyo, Tokyo 113-8656, Japan;* orcid.org/0000-0003-3548-5952

**Akira Yamakata** − *Graduate School of Natural Science and Technology, Okayama University, Okayama 700-8530, Japan;* orcid.org/0000-0003-3179-7588

Complete contact information is available at:
https://pubs.acs.org/10.1021/jacs.6c03784

### Notes

The authors declare no competing financial interest.

## ■ ACKNOWLEDGMENTS

This work was supported by the Artificial Photosynthesis Project of the New Energy and Industrial Technology Development Organization (NEDO) and by the JSPS Program for Forming Japan's Peak Research Universities (J-PEAKS) through grant no. JPJS00420230007. This work was also supported by "Advanced Research Infrastructure for Materials and Nanotechnology in Japan (ARIM)" of the Ministry of Education, Culture, Sports, Science and Technology (MEXT) through no. JPMXP1225UT0095. Part of this research was funded through a joint research project with Shimadzu Corporation. X-ray absorption spectroscopy measurements were performed at the 4B7A and 4B7B beamlines of the Beijing Synchrotron Radiation Facility (BSRF) and at the BM44 beamline of the High Energy Photon Source (HEPS).

## ■ REFERENCES

(1) Hisatomi, T.; Domen, K. Reaction systems for solar hydrogen production via water splitting with particulate semiconductor photocatalysts. *Nat. Catal.* **2019**, *2*, 387−399.

(2) Yu, J.; Huang, J.; Li, R.; Li, Y.; Liu, G.; Xu, X. Fluorine-expedited nitridation of layered perovskite $Sr_2TiO_4$ for visible-light-driven photocatalytic overall water splitting. *Nat. Commun.* **2025**, *16*, No. 361.

(3) Li, Z.; Li, R.; Jing, H.; Xiao, J.; Xie, H.; Hong, F.; Ta, N.; Zhang, X.; Zhu, J.; Li, C. Blocking the reverse reactions of overall water splitting on a Rh/GaN−ZnO photocatalyst modified with $Al_2O_3$. *Nat. Catal.* **2023**, *6*, 80−88.

(4) Xiao, J.; Hisatomi, T.; Domen, K. Narrow-Band-Gap Particulate Photocatalysts for One-StepExcitation Overall Water Splitting. *Acc. Chem. Res.* **2023**, *56*, 878−888.

(5) Wu, H.; Qu, S.; Huang, Y. Bismuth Vanadate Capable of Driving One-Step-Excitation Photocatalytic Overall Water Splitting. *J. Am. Chem. Soc.* **2025**, *147*, 10829−10833.

(6) Zhang, J.; Liu, Y.; Dittrich, T.; Wang, Z.; Ji, P.; Li, M.; Ta, N.; Zhang, H.; Zhen, C.; Xu, Y.; Li, D.; Feng, Z.; Li, Z.; Luo, Y.; Cui, J.; Su, D.; Weng, Y.; Liu, G.; Wang, X.; Fan, F.; Li, C. Unveiling charge utilization mechanisms in ferroelectric for water splitting. *Nat. Commun.* **2025**, *16*, No. 1515.

(7) Kang, W.; Wei, R.; Yin, H.; Li, D.; Chen, Z.; Huang, Q.; Zhang, P.; Jing, H.; Wang, X.; Li, C. Unraveling Sequential Oxidation Kinetics and Determining Roles of Multi-Cobalt Active Sites on $Co_3O_4$ Catalyst for Water Oxidation. *J. Am. Chem. Soc.* **2023**, *145*, 3470−3477.

(8) Takata, T.; Jiang, J.; Sakata, Y.; Nakabayashi, M.; Shibata, N.; Nandal, V.; Seki, K.; Hisatomi, T.; Domen, K. Photocatalytic water splitting with a quantum efficiency of almost unity. *Nature* **2020**, *581*, 411−414.

(9) Chen, K.; Xiao, J.; Vequizo, J. J. M.; Hisatomi, T.; Ma, Y.; Nakabayashi, M.; Takata, T.; Yamakata, A.; Shibata, N.; Domen, K. Overall Water Splitting by a $SrTaO_2N$-Based Photocatalyst Decorated with an Ir-Promoted Ru-Based Cocatalyst. *J. Am. Chem. Soc.* **2023**, *145*, 3839−3842.

(10) Chen, K.; Xiao, J.; Hisatomi, T.; Domen, K. Transition-metal (oxy)nitride photocatalysts for water splitting. *Chem. Sci.* **2023**, *14*, 9248−9257.

(11) Li, H.; Xiao, J.; Vequizo, J. J. M.; Hisatomi, T.; Nakabayashi, M.; Pan, Z.; Shibata, N.; Yamakata, A.; Takata, T.; Domen, K. One-Step Excitation Overall Water Splitting over a Modified Mg-Doped $BaTaO_2N$ Photocatalyst. *ACS Catal.* **2022**, *12*, 10179−10185.

(12) Nishimae, S.; Vequizo, J. J. M.; Inoue, Y.; Yamakata, A.; Nakabayshi, M.; Higashi, T.; Domen, K. Active $BaTaO_2N$ photocatalysts prepared from an amorphous $Ta_2O_5$ precursor for overall water splitting under visible light. *J. Mater. Chem. A* **2023**, *11*, 6299−6310.

(13) Xiao, J.; Nakabayashi, M.; Hisatomi, T.; Vequizo, J. J. M.; Li, W.; Chen, K.; Tao, X.; Yamakata, A.; Shibata, N.; Takata, T.; Inoue, Y.; Domen, K. Sub-50nm perovskite-type tantalum-based oxynitride single crystals with enhanced photoactivity for water splitting. *Nat. Commun.* **2023**, *14*, No. 8030.

(14) Wei, S.; Zhang, G.; Xu, X.; et al. Activating $BaTaO_2N$ by Ca modifications and cobalt oxide for visible light photocatalytic water oxidation reactions. *Appl. Catal., B* **2018**, *237*, 373−381.

(15) Wang, Z.; Luo, Y.; Hisatomi, T.; Vequizo, J. J. M.; Suzuki, S.; Chen, S.; Nakabayashi, M.; Lin, L.; Pan, Z.; Kariya, N.; Yamakata, A.; Shibata, N.; Takata, T.; Teshima, K.; Domen, K. Sequential cocatalyst decoration on $BaTaO_2N$ towards highly-active Z-scheme water splitting. *Nat. Commun.* **2021**, *12*, No. 1005.

(16) Zhang, H.; Wei, S.; Xu, X. Mg modified $BaTaO_2N$ as an efficient visible-light-active photocatalyst for water oxidation. *J. Catal.* **2020**, *383*, 135−143.

(17) Hojamberdiev, M.; Vargas, R.; Kadirova, Z. C.; Kato, K.; Sena, H.; Krasnov, A. G.; Yamakata, A.; Katsuya, T.; Lerch, M. Unfolding the Role of B Site-Selective Doping of Aliovalent Cations on Enhancing Sacrificial Visible Light-Induced Photocatalytic $H_2$ and $O_2$ Evolution over $BaTaO_2N$. *ACS Catal.* **2022**, *12*, 1403−1414.

(18) Hojamberdiev, M.; Vargas, R.; Kadirova, Z. C.; Teshima, K.; Lerch, M. Exploring the effect of partial B-site $Al^{3+}$−$Mg^{2+}$ dual substitution on optoelectronic, surface, and photocatalytic properties of $BaTaO_2N$. *Mater. Adv.* **2022**, *3*, 7348−7359.

(19) Lv, M.; Sun, X.; Wei, S.; Shen, C.; Mi, Y.; Xu, X. Ultrathin Lanthanum Tantalate Perovskite Nanosheets Modified by Nitrogen Doping for Efficient Photocatalytic Water Splitting. *ACS Nano* **2017**, *11*, 11441−11448.

(20) Chen, J. G. NEXAFS investigations of transition metal oxides, nitrides, carbides, sulfides and other interstitial compounds. *Surf. Sci. Rep.* **1997**, *30*, 1−152.

(21) de Groot, F. M. F. X-ray absorption and dichroism of transition metals and their compounds. *J. Electron Spectrosc. Relat. Phenom.* **1994**, *67*, 529−622.

(22) Kurata, H.; Lefevre, E.; Colliex, C. Electron-energy-loss near-edge structures in the oxygen E-edge spectra of transition-metal oxides. *Phys. Rev. B* **1993**, *47*, No. 13763.

(23) Johansson, L. I. Electronic and structural properties of transition-metal carbide and nitride surfaces. *Surf. Sci. Rep.* **1995**, *21*, 177−250.

(24) Noh, W.; Girolami, G. S. Synthesis and Characterization of the Cycloheptatrienyl Tantalum ″Mixed-Sandwich″ Compounds (C5R5)Ta(C7H7). *Inorg. Chem.* **2008**, *47*, 535−542.

(25) Nguyen, A. I.; Blackmore, K. J.; Carter, S. M.; Zarkesh, R. A.; Heyduk, A. F. One- and Two-Electron Reactivity of a Tantalum(V) Complex with a Redox-Active Tris(amido) Ligand. *J. Am. Chem. Soc.* **2009**, *131*, 3307−3316.

(26) Vequizo, J. J. M.; Kato, K.; Chen, S.; Hisatomi, T.; Wang, Z.; Takata, T.; Yamakata, A.; Domen, K. Boosted Photocatalytic Water Oxidation over $BaTaO_2N$ Produced from Perovskite Oxides Based on Photoinduced Charge Carriers. *Energy Fuels* **2025**, *39*, 6584−6591.

(27) Higashi, T.; Seki, K.; Sasaki, Y.; Pihosh, Y.; Nandal, V.; Nabayashi, M.; Shibata, N.; Domen, K. Mechanistic Insights into Enhanced Hydrogen Evolution of $CrO_x$/Rh Nanoparticles for Photocatalytic Water Splitting. *Chem. - Eur. J.* **2023**, *29*, No. e202204058.

(28) Chen, S.; Shen, S.; Liu, G.; Qi, Y.; Zhang, F.; Li, C. Interface Engineering of a $CoO_x$ /$Ta_3N_5$ Photocatalyst for Unprecedented Water Oxidation Performance under Visible-LightIrradiation. *Angew. Chem., Int. Ed.* **2015**, *127*, 3090−3094.